PHYSICAL REVIEW B **93**, 041421(R) (2016)

Observation of quantum Hall plateau-plateau transition and scaling behavior of the zeroth Landau level in graphene *p-n-p* junctions

Cheng-Hua Liu,[1,2] Po-Hsiang Wang,[2] Tak-Pong Woo,[1] Fu-Yu Shih,[1,2] Shih-Ching Liou,[1,2] Po-Hsun Ho,[3] Chun-Wei Chen,[3] Chi-Te Liang,[1] and Wei-Hua Wang[2,*]

[1]*Department of Physics, National Taiwan University, Taipei 106, Taiwan*

[2]*Institute of Atomic and Molecular Sciences, Academia Sinica, Taipei 106, Taiwan*

[3]*Department of Materials Science and Engineering, National Taiwan University, Taipei 106, Taiwan*

(Received 6 November 2015; revised manuscript received 4 January 2016; published 26 January 2016)

We report distinctive magnetotransport properties of a graphene *p-n-p* junction prepared by controlled diffusion of metallic contacts. In most cases, materials deposited on a graphene surface introduce substantial carrier scattering, which greatly reduces the high mobility of intrinsic graphene. However, we show that an oxide layer only weakly perturbs the carrier transport, which enables fabrication of a high-quality graphene *p-n-p* junction through a one-step and resist-free method. The measured conductance-gate voltage (G-V_G) curves can be well described by a metal contact model, which confirms the charge-density depinning due to the oxide layer. The graphene *p-n-p* junction samples exhibit a pronounced quantum Hall (QH) effect, a well-defined transition point of the zeroth Landau level (LL), and scaling behavior. The scaling exponent obtained from the evolution of the zeroth LL width as a function of temperature exhibits a relatively low value of $\kappa = 0.21 \pm 0.01$. Moreover, we calculate the energy level for the LLs based on the distribution of plateau-plateau transition points, further validating the assignment of the LL index of the QH plateau-plateau transition.

DOI: 10.1103/PhysRevB.93.041421

Electrical transport studies of graphene heterostructures [1] have revealed the quantum Hall effect (QHE) [2], quantum interference behaviors [3,4], Klein tunneling [5,6], and the split closed-loop resonator [7], hence convincingly demonstrating the advantages of constructing in-plane heterostructures of graphene. Specifically, the relativistic quantization of the electronic spectrum of graphene results in distinct characteristics, including the presence of a Landau level (LL) at zero energy and a chiral QHE [8–12]. In the quantum Hall (QH) regime, the plateau-plateau transition and the scaling behavior have been studied using Hall bar [13–18] and Corbino geometry [19], providing important information about the carrier localization in graphene. A scaling exponent for a typical Anderson-type transition $\kappa \cong 0.42$ has been reported in graphene [13,14], while some studies showed a reduced value of κ [15–19]. In a graphene Hall bar, the slope of the Hall conductivity at the transition region $d\sigma_{xy}/d\nu$ exhibits scaling behavior with $\kappa = 0.41$ for the first and second LLs, while that of the zeroth LL is temperature (T) independent [13]. In a Corbino geometry, the full width at half maximum (FWHM) $\Delta\nu$ of the zeroth LL is T dependent and shows scaling behavior with $\kappa = 0.16$, which is attributed to an inhomogeneous charge carrier distribution [19]. However, until now, a well-defined QH plateau-plateau transition point of the zeroth LL of graphene has not been directly observed, obscuring a detailed understanding of the scaling behavior of this unique LL. Moreover, the variation of the T exponent in previous reports suggests the need for further investigation of the scaling behavior of the zeroth LL using different methods for the device structures.

In this Rapid Communication, we fabricate a high-quality graphene *p-n-p* junction, achieved via controlled diffusion of metallic contacts, to explore the QH plateau-plateau transition and scaling behavior of graphene. Interestingly, we observe a well-defined transition point corresponding to the zeroth LL, revealing the scaling behavior and a reduced T exponent. There are additional advantages of utilizing a graphene *p-n-p* junction to explore the transition region of the QHE. First, the presence of the transition between an integer QH plateau and a QH plateau with a fractional value enables direct access of the transition of the zeroth LL. Second, in a graphene *p-n-p* geometry, the intrinsic graphene is adjoined by the doped graphene from both sides. The doped graphene regions can be viewed as an ideal contact, facilitating the investigation of the transition region of the intrinsic graphene. Moreover, we derive the value of energy level for the observed LLs, which agrees with the theoretical values, further validating the assignment of the LL index of the QH plateau-plateau transition.

A detailed device fabrication process can be found in Supplemental Material S1 [20]. Briefly, we exfoliated graphene onto the SiO_2/Si substrates modified by the organic molecule octadecyltrichlorosilane (OTS), which can greatly reduce charged-impurity scattering and provide an ultrasmooth substrate surface [21]. We then employed resist-free fabrication with a shadow mask to reduce possible polymer residue. A crucial step in this process was to control the metal diffusion of electrodes by deliberately increasing the gap between the shadow mask and graphene samples [22]. Figure 1(a) shows a schematic of the graphene *p-n-p* junction device with a pronounced diffusion of the metallic contact. With a gap of 130 ± 5 μm, we deposited 5-nm-thick Ti and 50-nm-thick Au as contact electrodes, which resulted in a large lateral diffusion of approximately 4 μm, as evidenced by an atomic force microscopy (AFM) image of sample A [Fig. 1(b), blue gradient area]. Before the transport/magnetotransport measurement, the samples were annealed at 383 K for 3 h in a low vacuum (helium atmosphere) to remove adsorbates [21].

We note the critical role of the Ti layer in determining the transport behavior by comparing the two-terminal conductance

*Author to whom correspondence should be addressed: wwang@sinica.edu.tw

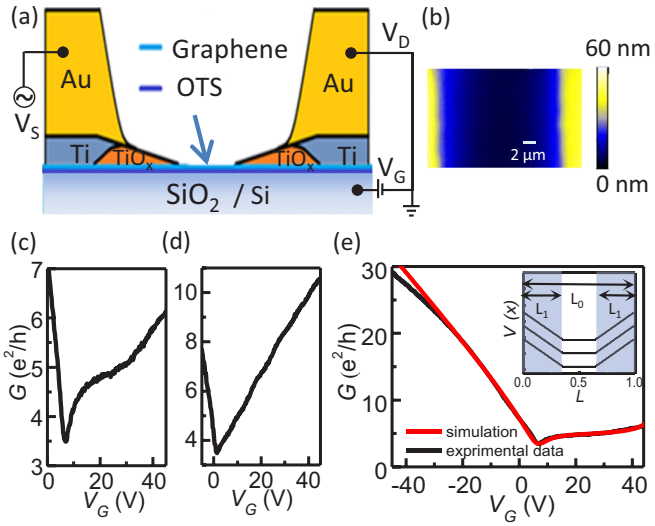

FIG. 1. The structure and the transport characteristics of the graphene p-n-p junctions. (a) A schematic of the structure of the graphene device with diffused electrode edges. (b) An AFM image showing the edge diffusion of sample A. Comparison of the G-V_G curves between (c) sample A and (d) sample B with Au electrode. (e) Measured G-V_G curve for sample A at $T = 2$ K and simulation based on the metal contact model. Inset: Depinning potential assumed in the simulation.

versus gate voltage (G-V_G) curves of a graphene p-n-p junction (sample A) and a control sample (sample B), as shown in Figs. 1(c) and 1(d), respectively. For sample A, a large field effect is observed for $V_G < 7$ V, showing a typical graphene characteristic, in which the G-V_G curve can be well described by the self-consistent Boltzmann equation $\rho = (ne\mu_c + \sigma_0)^{-1} + \rho_s$, where μ_c, ρ_s, and σ_0 are density-independent mobility, the resistivity due to short-range scattering, and residual conductance at the Dirac point, respectively. The fitting yields that μ_c and ρ_s of sample A are 3000 cm^2/V s and 368 Ω, respectively. However, the G-V_G curve for $V_G > 7$ V shows an additional conductance minimum at $V_G = 32$ V, suggesting a doping effect of graphene in the diffused electrode region [23,24] (Supplemental Material S2). The double conductance minimum was observed in other graphene p-n-p junction devices, as shown in Supplemental Material S3. To examine the role of the Ti layer, we have fabricated sample B such that the contact metal is made only with Au instead of the Ti/Au bilayer. Different from sample A, sample B exhibits a typical G-V_G curve in the regime $V_G > V_{CNP}$, as shown in Fig. 1(d). We therefore infer that the double dip feature observed in sample A is related to the Ti adhesion layer.

It is well understood that the charge density of graphene under metallic contact is pinned due to Fermi level pinning [25,26], leading to typical transfer characteristics. Nevertheless, an additional kink is observed in the G-V_G curve, suggesting that the depinning of charge density occurs [27,28]. We performed a theoretical simulation of the G-V_G curves based on a simple metal contact model [27] (Supplemental Material S4). By assuming charge-density depinning and employing the potential profile $V(x)$ depicted in the inset of Fig. 1(e), we calculated transfer characteristics that reasonably fit the measured data, as shown in Fig. 1(e). The agreement between the modeled and the measured G-V_G curve suggests that the interfacial metal is oxidized [28]. In the calculation, we applied the device geometry with $L_0/W = 1.06$ and assumed $L_1 = 0.35L_0$ ($L_0 = 12$ μm). We note that the resulting $L_1 = 4.2$ μm is comparable to the diffusion length of 4 μm obtained from the AFM images [Fig. 1(b)], indicating that the interfacial oxidation occurs approximately in the diffused area. The depinning enables large-area modification of the carrier density [27,28], which causes a doped graphene region [29]. We therefore conclude that charge-density depinning and the doping effect occur in the diffusion region, leading to a graphene p-n-p structure.

We present the magnetotransport properties of the fabricated graphene p-n-p junctions. Figure 2(a) compares the G-V_G curves of sample A at $B = 0$ and 9 T. The graphene sample exhibits two conductance minima at $B = 0$ T, corresponding to the pristine and doped graphene regions mentioned above. Therefore, sample A is in the unipolar regime for $V_G < 7$ V and $V_G > 32$ V and in the bipolar regime for 7 V $< V_G <$ 32 V. At $B = 9$ T, sample A manifests a pronounced QHE, revealing QH plateaus for $\nu = 2$, 6, and 10 in the unipolar regime and a QH plateau at $\nu = 2/3$ in the bipolar regime. In a graphene p-n-p junction, the direction of the chiral edge states under a magnetic field is determined by the types of carriers. In the bipolar regime, these chiral states

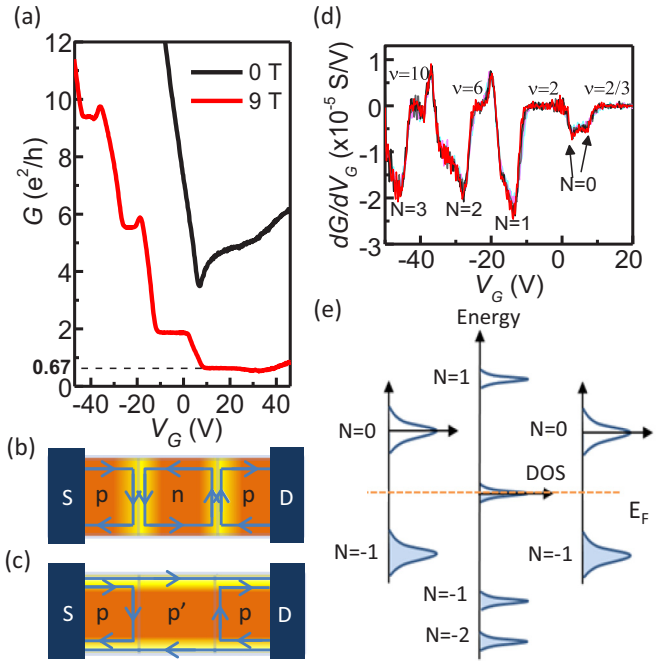

FIG. 2. The magnetotransport of the graphene p-n-p junctions. (a) The G-V_G curves of sample A at $B = 0$ T (black) and $B = 9$ T (red). (b), (c) Edge state circulation of the graphene p-n junctions in the QH regime. (b) Edge currents in p and n regions, which circulate in opposite directions and mix at the p-n interface in the bipolar regime. (c) Edge currents in the unipolar regime, which circulate in the same direction. (d) The differential conductance as a function of V_G, indicating the plateau-plateau transition points. (e) A schematic of the energy distribution of the LLs of the graphene p-n-p junction.

circulate with opposite direction in p- and n-type regions, as shown in the schematic of Fig. 2(b). When the edge states form a compressible channel at the p-n interface with full mixing equilibrium [2], the conductance can be expressed as $G = \nu_{pnp} e^2/h$, with $\nu_{pnp} = |\nu_1||\nu_2|/(|\nu_1| + 2|\nu_2|)$ ($\nu_1\nu_2 < 0$, $\nu_1, \nu_2 = \pm 2, \pm 6, \pm 10 \ldots$) The mixture of $\nu_1 = 2$ of the intrinsic graphene region and $\nu_2 = -2$ of the doped region results in the observed $\nu = 2/3$ of the first mixing filling factor. We note that the carriers can propagate through the graphene p-n interface with suppressed backscattering known as Klein tunneling [3,5], which may facilitate the observed full mixing of the edge states. In the unipolar regime, the filling factor is given by $G = \min(|\nu_1|, |\nu_2|)\frac{e^2}{h}$, which can account for the integer QH plateau of $\nu = 2$, 6, and 10. The edge states circulate in the same direction in all three regions and only the edge states that permeate the whole channel contribute to the measured G. The edge states that propagate across the interface are nondissipative due to the suppressed backscattering [30]. It is noted that the observation of the fractional-valued QH plateaus is irrelevant to the fractional QH effect due to the formation of complex composite quasiparticles [31,32], but is originated from the merging of the edge state at the p-n interface.

In Supplemental Material S3, we show two other graphene p-n-p junction devices (samples C and D), which exhibit a comparable QHE, indicating the validity of the fabrication method. We note that despite the presence of charged-impurity scattering introduced by the oxide layer, the high mobility and the QH regime can still be attained in our graphene samples. To evaluate the disorder in our graphene p-n-p junction devices, we calculate the Ioffe-Regel parameter $(k_F\lambda)^{-1}$, where λ is the transport mean free path, yielding $(k_F\lambda)^{-1} = 0.5$, 0.3, and 0.4 for samples A, C, and D, respectively. The obtained $(k_F\lambda)^{-1} < 1$ indicates that the graphene p-n-p junction samples have reasonably low disorder. Furthermore, Fig. 2(d) shows the derivative of dG/dV_G as a function of V_G for 2 K $< T <$ 100 K. We note that the minimum for the zeroth LL exhibits split peaks, while the minima for other LLs only show a single peak. The presence of the split peaks of the zeroth LL may be attributed to sublattice symmetry breaking in the samples with a small disorder strength [33], which is consistent with the aforementioned low disorder of the sample.

A schematic diagram of the energy level of the LLs in the graphene p-n-p junction is shown in Fig. 2(e). Because of the extra carriers induced by the p-type doping, the energy of the LLs in the doped region is higher than that of the same LL index in the intrinsic region. We note that the device does not show a transition when the Fermi level crosses the LLs of the doped graphene because the chiral edge states in those regions reflect back to the same electrodes [see the schematics of Figs. 2(b) and 2(c)] and do not contribute to the two-terminal resistance. Therefore, the transition of the QHE is only manifested by the LLs of the intrinsic graphene. The doped graphene regions thus act as a contact in this sense, offering a unique means to probe the LLs of the intrinsic graphene.

We further discuss the robustness of the QH state against the thermal energy. Figure 3(a) shows the G-V_G curves for 2 K $<$ $T <$ 100 K. At $T = 2$ K, the sample exhibits pronounced QH plateaus at $\nu = 2$, 6, and 10 and $\nu = 2/3$ for the unipolar and bipolar regime, respectively. The QH plateau at $\nu = 2$ is

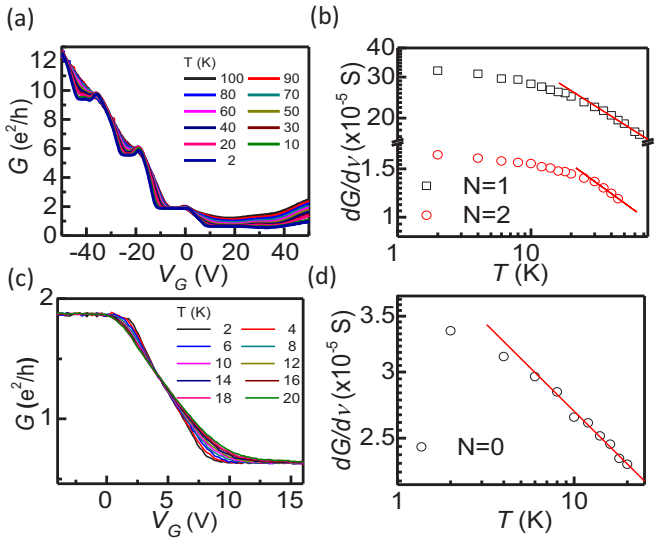

FIG. 3. The scaling behavior of the QH plateau-plateau transitions. (a) The G-V_G curves of sample A from $T = 2$ K to $T = 100$ K. (b) $(dG/d\nu)_{\max}$ as a function of T and the fits, which yield the scaling exponent for the first and second LLs. (c) The G-V_G curves of sample A from $T = 2$ to 20 K, exhibiting the transition region between the integer QH plateau $\nu = 2$ and the fractional-valued QH plateau $\nu = 2/3$. (d) $(dG/d\nu)_{\max}$ as a function of T and the fitting of the scaling exponent for the zeroth LL.

particularly robust, persisting up to $T = 100$ K. Conversely, the QH plateaus at $\nu = 6$ and 10 and $\nu = 2/3$ are further subjected to the influence of the thermal energy. The energy quantization of graphene in a magnetic field can be written as $E_N = \nu_F\sqrt{|\,2e\hbar BN\,|}$, where ν_F is the Fermi velocity and N is the LL index. The energy gap of the QH plateau at $\nu = 2$ can be estimated as $\Delta E = E_1 - E_0 \approx 1000$ K at $B = 9$ T. Because the cyclotron gap $\hbar\omega_c$ is larger than the thermal energy K_BT by a factor of 10 [34], the persistence of the QH plateau at $\nu = 2$ for $T < 100$ K, which is comparable to the observed critical T, is implied. Alternatively, the energy gap of the fractional-valued QH plateau at $\nu = 2/3$ is smaller than that of the QH plateau at $\nu = 2$ [see Fig. 2(e)], causing a weaker persistence of the QHE against thermal excitation.

We now focus on the scaling behavior of the QH plateau-plateau transitions in our graphene p-n-p junction devices. In the QH regime, both the localized and extended states are critical to the development of the QHE, and the width of the QH plateaus depends on the ratio of localized to extended states [35]. At the QH plateau-plateau transition, the presence of the delocalized states results in nonzero σ_{xx}; σ_{xy} becomes nonquantized because these states condense into a fluid state, leading to a transition region of nonzero width between quantized values [36]. The delocalization can be manifested by the scaling behavior of the magnetoresistance (MR) as a function of T in the transition region [37], which can be inferred as follows. In the center of a LL, the localization length ξ of electronic states diverges as $\xi \propto |\nu - \nu_c|^{-\gamma}$, where ν_c is the LL center and ν is its localization edge [38]. It can then be derived that the maximum slope of $d\sigma_{xy}/d\nu$ diverges as $T^{-\kappa}$ in the transition region, with the exponent $\kappa = p/2\gamma$, where γ is the localization length exponent and p is the inelastic

scattering exponent [37,38]. Hence, the deviation of the field from its critical value ($\nu - \nu_c$) rescales by the factor T^κ as T decreases; it follows that the transition region becomes smaller as T decreases.

From Fig. 3(a), we can extract $(dG/d\nu)_{\max}$, the maximum of the slope for each T, in which the filling factor ν is calculated using the relation $\nu = nh/eB$. We can then plot the T dependence of $(dG/d\nu)_{\max}$ for the first and second LLs corresponding to the intrinsic region of the p-n-p junction, as shown in Fig. 3(b). The value of $(dG/d\nu)_{\max}$ is extracted up to the T value at which the QH plateaus are about to disappear. Sample A exhibits a scaling behavior, and $(dG/d\nu)_{\max}$ varies linearly with T for 30 K $< T <$ 70 K, yielding $\kappa = 0.36 \pm 0.01$ and 0.35 ± 0.01 for the first and second LLs, respectively. In this study, we measured the two-terminal G composed of both σ_{xx} and σ_{xy} components, which may complicate the analysis of the MR. However, we note that the discussions of the scaling behavior and the extraction of the slope $dG/d\nu$ are restricted in the plateau-plateau transition of the intrinsic region [see Fig. 2(e)], while both σ_{xx} and σ_{xy} corresponding to the doped region are within the QH plateau regime and do not affect the value of G. Moreover, although σ_{xx} is not zero at the transition of the intrinsic region, it is around the maximum value where $(dG/d\nu)_{\max}$ occurs and contributes insignificantly to $dG/d\nu$. Therefore, the measured alteration of the slope $dG/d\nu$ is dominated by the T dependence of σ_{xy}, which validates the analysis of the scaling behavior of the QH plateau-plateau transition by using two-terminal geometry.

Here, we assume that $p = 2$, which is generally accepted for a two-dimensional (2D) system dominated by short-range scattering. This is conceivable because the carrier transport is dominated by short-range scattering for TiO_2 on graphene [39]. From the relation $\kappa = p/2\gamma$, we then obtain $\gamma = 2.7$, which is in reasonable agreement with the theoretical calculation $\gamma = 2.35$ [35], indicating that localization of the higher-order LLs in our graphene p-n-p samples is governed by a scaling behavior similar to that in conventional 2D systems. At lower T, the T dependence of $(dG/d\nu)_{\max}$ becomes smaller because the localization length approaches the intrinsic scattering length, which is T independent [19]. We define T_C as the T where the data start to deviate from the scaling behavior. It is found that T_C for the first and second LLs are comparable (approximately 30 K), suggesting that T_C is associated with the dimension of the sample but not the LL index.

Notably, we observe the scaling behavior of the QH plateau-plateau transition between integer and fractional-valued QH plateaus of graphene. Figure 2(c) shows the G-V_G curves at the transition region between the integer QH plateau $\nu = 2$ and the fractional-valued QH plateau $\nu = 2/3$ for T ranging from 2 to 20 K. According to the energy levels of the LLs shown in Fig. 2(e), this transition occurs at the zeroth LL of the intrinsic graphene region. We obtain $\kappa = 0.21 \pm 0.01$ for the zeroth LL, which is smaller than those of the first and second LLs. A reduced value of κ for the zeroth LL has been reported in the graphene Corbino device [19], which has been attributed to the dominance of electron-hole puddles, as evidenced by an inhomogeneous charge carrier distribution [13,19]. Because the transition of the zeroth LL coincides with the charge neutrality point, the reduced κ observed in the graphene p-n-p junction may be related to the presence of the electron-hole puddles [40].

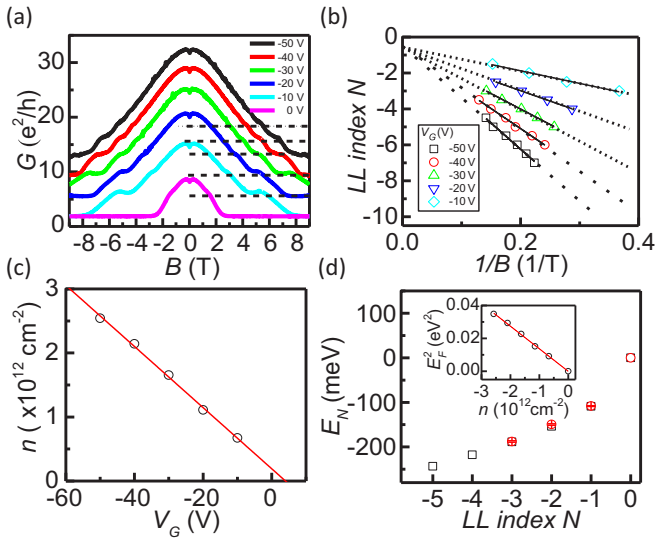

FIG. 4. The MR and the distribution of the energy levels of the LLs. (a) The MR, showing SdH oscillations in the unipolar regime. (b) A fan diagram showing the LL index as a function of $1/B_N$ at different V_G. (c) The carrier concentration $n = 4e/hB_F(V_G)$, which is linearly dependent on V_G, from which the carrier density capacitance is extracted. (d) The energy of the Nth LL (E_N) as a function of the LL index. Inset: Fermi energy as a function of carrier density.

Finally, we estimate the energy level (E_N) for the LL index to validate the assignment of the LLs of the QH plateau-plateau transition. Figure 4(a) shows the MR curves of sample A for different V_G in the unipolar regime. At -0.3 T $< B <$ 0.3 T, we observe negative MR, which can be attributed to weak localization (WL) [41,42]. Beyond the WL regime, sample A exhibits positive MR, which can be explained by the classical Hall effect. Moreover, we observe oscillating peaks, which are coupled by the Shubnikov–de Haas (SdH) oscillations in σ_{xx} for -50 V $< V_G <$ -10 V. For $V_G = 0$ V, sample A enters the QH regime for $B > 3$ T and manifests a pronounced QH plateau at $\nu = 2$, which is consistent with the aforementioned QHE. We then construct the Landau fan diagram by identifying the value of the $1/B_N$ field corresponding to the Nth maxima and minima of the SdH oscillations and by plotting against the Landau index N at different V_G, as shown in Fig. 4(b). The N vs $1/B_N$ data at different V_G can be fitted linearly, and these lines extrapolate and converge at -0.5 of the y axis, indicating a nonzero Berry phase of monolayer graphene [10]. From the slope of the linear fitting, we can obtain the SdH oscillation period $1/B_F(V_G)$, yielding the V_G dependence of carrier density as $n = 4e/hB_F(V_G)$, which is shown in Fig. 4(c). We found that n varies linearly with V_G, and the capacitance of the graphene device on 300-nm-thick SiO_2 is calculated as $\alpha = n(V_G)/V_G = 4.77 \times 10^{10}$ cm^{-2} V^{-1}.

From the Landau fan diagram, the relationship between E_F and $n(V_G)$ can be derived using $B_F = E_F^2/2e\nu_F{}^2\hbar$ [43–45], where $\nu_F = 10^6$ m/s, as shown in the inset of Fig. 4(d). We note that E_F varies linearly with the square root of n, which is consistent with the behavior of relativistic Dirac particles described by $E_F = \hbar\nu_F\kappa_F = \hbar\nu_F\sqrt{n\pi}$ [46,47]. We

then identify $V_G(\nu)$ for the LL index based on the corresponding derivative minima from dG/dV_G vs V_G curves [Fig. 2(d)]. By converting $V_G(\nu)$ to $n(\nu)$ and using the E_F-n relation, we obtain the E_N corresponding to the LL index, as shown in Fig. 4(d). The estimated E_N versus the LL index agrees well with theoretically derived values based on $E_N = v_F\sqrt{2e\hbar BN}$ with $B = 9$ T, indicating the validity of the assignment of the LLs of the QH plateau-plateau transition.

In summary, we demonstrated a unique method of fabricating a graphene p-n-p junction by controlling the lateral diffusion of the metallic contacts. The measured G-V_G curves can be thoroughly described by the metal contact model, confirming the charge-density depinning and the presence of interfacial oxidation. The graphene p-n-p junction devices showed a pronounced QHE, a well-defined transition point of the zeroth LL, and the scaling behavior. We also estimated E_N for the LL index which is consistent with the theoretically derived values. The demonstration of a high-quality graphene p-n-p junction with controlled diffusion of the contacts provides an alternative fabrication method for future graphene-based electronics.

This work was supported by the Ministry of Science and Technology of Taiwan under Contracts No. MOST 103-2112-M-001-020-MY3 and No. MOST 104-2622-8-002-003.

[1] A. F. Young and P. Kim, Annu. Rev. Condens. Matter Phys. **2**, 101 (2011).
[2] B. Ozyilmaz, P. Jarillo-Herrero, D. Efetov, D. A. Abanin, L. S. Levitov, and P. Kim, Phys. Rev. Lett. **99**, 166804 (2007).
[3] A. F. Young and P. Kim, Nat. Phys. **5**, 222 (2009).
[4] M. Satoru, M. Sei, O. Masahiro, I. Kazuyuki, W. Kenji, T. Takashi, and M. Tomoki, Jpn. J. Appl. Phys. **52**, 110105 (2013).
[5] M. I. Katsnelson, K. S. Novoselov, and A. K. Geim, Nat. Phys. **2**, 620 (2006).
[6] A. V. Shytov, M. S. Rudner, and L. S. Levitov, Phys. Rev. Lett. **101**, 156804 (2008).
[7] Z. Liu *et al.*, Nat. Nanotechnol. **8**, 119 (2013).
[8] A. K. Geim and K. S. Novoselov, Nat. Mater. **6**, 183 (2007).
[9] K. S. Novoselov, A. K. Geim, S. V. Morozov, D. Jiang, M. I. Katsnelson, I. V. Grigorieva, S. V. Dubonos, and A. A. Firsov, Nature (London) **438**, 197 (2005).
[10] Y. Zhang, Y.-W. Tan, H. L. Stormer, and P. Kim, Nature (London) **438**, 201 (2005).
[11] K. S. Novoselov, E. McCann, S. V. Morozov, V. I. Fal'ko, M. I. Katsnelson, U. Zeitler, D. Jiang, F. Schedin, and A. K. Geim, Nat. Phys. **2**, 177 (2006).
[12] A. H. Castro Neto, F. Guinea, N. M. R. Peres, K. S. Novoselov, and A. K. Geim, Rev. Mod. Phys. **81**, 109 (2009).
[13] A. J. M. Giesbers, U. Zeitler, L. A. Ponomarenko, R. Yang, K. S. Novoselov, A. K. Geim, and J. C. Maan, Phys. Rev. B **80**, 241411 (2009).
[14] T. Shen, A. T. Neal, M. L. Bolen, J. J. Gu, L. W. Engel, M. A. Capano, and P. D. Ye, J. Appl. Phys. **111**, 013716 (2012).
[15] C. Cobaleda, S. Pezzini, A. Rodriguez, E. Diez, and V. Bellani, Phys. Rev. B **90**, 161408 (2014).
[16] B. Jabakhanji, A. Michon, C. Consejo, W. Desrat, M. Portail, A. Tiberj, M. Paillet, A. Zahab, F. Cheynis, F. Lafont, F. Schopfer, W. Poirier, F. Bertran, P. Le Fèvre, A. Taleb-Ibrahimi, D. Kazazis, W. Escoffier, B. C. Camargo, Y. Kopelevich, J. Camassel, and B. Jouault, Phys. Rev. B **89**, 085422 (2014).
[17] M. Amado, E. Diez, F. Rossella, V. Bellani, D. Lopez-Romero, and D. K. Maude, J. Phys.: Condens. Matter **24**, 305302 (2012).
[18] E. Pallecchi, M. Ridene, D. Kazazis, F. Lafont, F. Schopfer, W. Poirier, M. O. Goerbig, D. Mailly, and A. Ouerghi, Sci. Rep. **3**, 1791 (2013).
[19] E. C. Peters, A. J. M. Giesbers, M. Burghard, and K. Kern, Appl. Phys. Lett. **104**, 203109 (2014).
[20] See Supplemental Material at http://link.aps.org/supplemental/10.1103/PhysRevB.93.041421 for device fabrication and electrical measurement, transport/magnetotransport properties of the control samples, characteristics of graphene p-n-p junction devices, theoretical simulation based on metal contact model.
[21] S. Y. Chen, P. H. Ho, R. J. Shiue, C. W. Chen, and W. H. Wang, Nano Lett. **12**, 964 (2012).
[22] C.-H. Liu, P.-H. Wang, S.-C. Liou, P.-H. Ho, C.-W. Chen, C.-T. Liang, and W.-H. Wang (unpublished).
[23] J. R. Williams, L. DiCarlo, and C. M. Marcus, Science **317**, 638 (2007).
[24] H. C. Cheng, R. J. Shiue, C. C. Tsai, W. H. Wang, and Y. T. Chen, ACS Nano **5**, 2051 (2011).
[25] B. Huard, N. Stander, J. A. Sulpizio, and D. Goldhaber-Gordon, Phys. Rev. B **78**, 121402 (2008).
[26] T. Mueller, F. Xia, M. Freitag, J. Tsang, and P. Avouris, Phys. Rev. B **79**, 245430 (2009).
[27] R. Nouchi and K. Tanigaki, Appl. Phys. Lett. **96**, 253503 (2010).
[28] R. Nouchi and K. Tanigaki, Appl. Phys. Lett. **105**, 033112 (2014).
[29] F. N. Xia, V. Perebeinos, Y. M. Lin, Y. Q. Wu, and P. Avouris, Nat. Nanotechnol. **6**, 179 (2011).
[30] D. A. Abanin and L. S. Levitov, Science **317**, 641 (2007).
[31] X. Du, I. Skachko, F. Duerr, A. Luican, and E. Y. Andrei, Nature (London) **462**, 192 (2009).
[32] K. I. Bolotin, F. Ghahari, M. D. Shulman, H. L. Stormer, and P. Kim, Nature (London) **462**, 196 (2009).
[33] F. Ortmann and S. Roche, Phys. Rev. Lett. **110**, 086602 (2013).
[34] K. S. Novoselov *et al.*, Science **315**, 1379 (2007).
[35] B. Huckestein, Rev. Mod. Phys. **67**, 357 (1995).
[36] S. L. Sondhi, S. M. Girvin, J. P. Carini, and D. Shahar, Rev. Mod. Phys. **69**, 315 (1997).
[37] H. P. Wei, D. C. Tsui, M. A. Paalanen, and A. M. M. Pruisken, Phys. Rev. Lett. **61**, 1294 (1988).
[38] A. M. M. Pruisken, Phys. Rev. Lett. **61**, 1297 (1988).
[39] K. M. McCreary, K. Pi, and R. K. Kawakami, Appl. Phys. Lett. **98**, 192101 (2011).
[40] J. Martin, N. Akerman, G. Ulbricht, T. Lohmann, J. H. Smet, K. Von Klitzing, and A. Yacoby, Nat. Phys. **4**, 144 (2008).

[41] S. V. Morozov, K. S. Novoselov, M. I. Katsnelson, F. Schedin, L. A. Ponomarenko, D. Jiang, and A. K. Geim, Phys. Rev. Lett. **97**, 016801 (2006).
[42] P. H. Wang *et al.*, Carbon **93**, 353 (2015).
[43] I. A. Luk'yanchuk and Y. Kopelevich, Phys. Rev. Lett. **93**, 166402 (2004).
[44] D. E. Soule, J. W. McClure, and L. B. Smith, Phys. Rev. **134**, A453 (1964).
[45] C. Berger *et al.*, Science **312**, 1191 (2006).
[46] P. R. Wallace, Phys. Rev. **71**, 622 (1947).
[47] G. P. Mikitik and Y. V. Sharlai, Phys. Rev. Lett. **82**, 2147 (1999).